

Searching for Variable Stars in the Open Cluster NGC 2355 and Its Surrounding Region

HONG WANG,^{1,2} YU ZHANG,^{1,2} XIANGYUN ZENG,³ QINGSHUN HU,^{1,2} JINZHONG LIU,^{1,2} MINGFENG QIN,^{1,2} AND GUOLIANG LÜ⁴

¹*Xinjiang Astronomical Observatory, Chinese Academy of Sciences, Urumqi, Xinjiang 830011, People's Republic of China*

²*School of Astronomy and Space Science, University of Chinese Academy of Sciences, Beijing 100049, People's Republic of China*

³*Center for Astronomy and Space Sciences, China Three Gorges University, Yichang 443000, People's Republic of China*

⁴*School of Physical Science and Technology, Xinjiang University, Urumqi, 830064, People's Republic of China*

ABSTRACT

We have investigated the variable stars in the field surrounding NGC 2355 based on the time-series photometric observation data. More than 3000 CCD frames were obtained in the *V* band spread over 13 nights with the Nanshan One-meter Wide-field Telescope. We have detected 88 variable stars, containing 72 new variable stars and 16 known variable stars. By analyzing these light curves, we classified the variable stars as follows: 26 eclipsing binaries, 52 pulsating stars, 4 rotating variables, and 6 unclear type variable stars for which their periods are much longer than the time baseline chosen. Employing *Gaia* DR2 parallax, kinematics, and photometry, the cluster membership of these variable stars were also analyzed for NGC 2355. In addition to the 11 variable members reported by Cantat-Gaudin et al. (2018), we identify 4 more variable member candidates located at the outer region of NGC 2355 and showed homogeneity in space positions and kinematic properties with the cluster members. The main physical parameters of NGC 2355 estimated from the two-color and color-magnitude diagrams are $\log(\text{age/yr}) = 8.9$, $E(B - V) = 0.24$ mag, and $[\text{Fe}/\text{H}] = -0.07$ dex.

Keywords: Galaxy — open cluster: individual: NGC 2355 — stars: variables: general — technique: photometric — method: data analysis

1. INTRODUCTION

Open clusters are exceptional laboratories for us to understand the fundamental astrophysical processes and one of the principal components of the Galaxy. It is believed that a significant number of stars in the Galaxy are formed in clusters (Joshi et al. 2020). Therefore, their extensive study is vital to infer the star formation history in the Galaxy (Phelps & Janes 1994) and to probe the Galactic structure (Chen et al. 2003; Cantat-Gaudin et al. 2018). Chemical abundance, age, spatial distribution, and kinematic characteristics of open clusters are the main keys to studying the formation and evolution of stars, clusters, and Galactic disc. Generally, most of the stars in the clusters exist in a variational form, and their luminosity changes chiefly for their internal reasons as well as external factors. The study of variable stars can provide a great deal of extra information that allows us to tighten the screws on theoretical models attempting to predict stellar properties, such as mass, radius, brightness, temperature, internal and external structure, some of which are difficult or impossible to

obtain in stars other than variable stars (Piskunov et al. 2006; Sandquist et al. 2011).

The open cluster NGC 2355 [RA(J2000.0) = 07^h16^m59.3^s, Dec(J2000.0) = 13°46′19″] is situated in the anti-center direction of the Galaxy, in the constellation of Gemini. In one of the earliest studies of NGC 2355, a photometric survey in *U*, *B*, *V* bands down to $V \sim 18.1$ mag was taken by Kaluzny & Mazur (1991) with the 0.9-m telescope at Kitt Peak National Observatory and they estimated the reddening of NGC 2355 to be $E(B - V) = 0.12$ mag, the distance modulus $(m - M)_0 = 12.1$, and the metallicity was +0.13 dex. Ann et al. (1999) examined open cluster NGC 2355 as a part of the Bohyunsan Optical Astronomy Observatory photometric survey in Korea and determined the $[\text{Fe}/\text{H}] = -0.32$ dex, $E(B - V) = 0.25$ mag, $(m - M)_0 = 11.4$ mag and age of 1 Gyr from *U*, *B*, *V*, *I* photometry by Doyak 1.8m telescope subsequently. Based on the two previously mentioned studies, Oliveira et al. (2013) used a method for estimating the metallicity of open clusters via non-subjective isochrone fitting using the cross-entropy global optimization algorithm applied to *U*, *B*, *V* photometric data. There was a disagreement in their work due to the two different extinction groups, the former with the age of 0.8 Gyr, the reddening of 0.22 mag, and the metallicity of -0.23 dex, while the latter with the age of 0.9 Gyr, $E(B - V) = 0.32$

mag and $[\text{Fe}/\text{H}] = -0.32$ dex. More recently, high-resolution spectra had been obtained for particular stars in or around the open cluster NGC 2355 by Soubiran et al. (2000), Jacobson et al. (2011), and Donati et al. (2015), and more precise metallicity were derived, approximately -0.06 to -0.08 dex.

However, to our knowledge, few studies researched the detailed variables for the open cluster NGC 2355, but only at the stage of photometry and spectroscopy for the cluster properties and parameters. This also provides an additional opportunity to characterize variable stars in this open cluster. In our work, we carry out an extensive search for variable stars in NGC 2355. The framework of this paper is structured as follows: observations and the data reduction procedures are presented in Section 2. We describe the circumstantial classification of variable stars in Section 3. In Section 4, we focus on the membership of the variable member stars and the stellar parameters associated with this open cluster, and we have also discussed the possibility of variable stars being missing cluster members. We present a summary of results in Section 5.

2. OBSERVATIONS AND DATA REDUCTIONS

All of the photometric observations for our study were taken with the Nanshan One-meter Wide-field Telescope (NOWT) at the Nanshan station of the Xinjiang Astronomical Observatory. The camera is equipped with an E2V 4160×4136 CCD203-82 with the pixel size of $12\ \mu\text{m}$ near the center of the CCD clip, yielding a scale of $1.125''$ per pixel and corresponding to a 78×78 arcmin² field of view around the center of the open cluster NGC 2355. The CCD operates at about $-120\ ^\circ\text{C}$ with liquid nitrogen cooling thus the dark current is less than $1\ e^- \text{pix}^{-1} \text{h}^{-1}$ at $-120\ ^\circ\text{C}$. To identify variable stars in NGC 2355, time-series observations were taken in the V band of the Johnson-Cousin-Bessel during 13 nights from January 8 to 10 in 2018 and December 10 to 19 in 2020 (Johnson & Morgan 1953; Cousins 1976; Bessell 1990). The detailed log of the observations is listed in Table 1. To secure photometric calibration of the CCD system, the standard star fields J005945 + 440830 and J234139 + 453900 (Clem & Landolt 2016), together with NGC 2355 were also observed in U, B, V, R, I bands on the night of 2018 January 9, as summarized in Table 2. Several biases and twilight flat-field frames were also taken in U, B, V, R , and I during the observing night.

The IRAF¹ package was used for pre-processing of data frames which include bias subtraction and flat-field correction (Tody 1986, 1993). To identify objects in the CCD

frames, the pixel coordinates of the frames were converted into equatorial coordinates by matching with the third US Naval Observatory CCD Astrograph Catalog (UCAC3). For all of the CCD frames we obtained, the photometry was carried out by SExtractor² SExtractor is a program that can perform reasonably well on astronomical images of moderately crowded star fields such as open clusters. It uses the K- σ Clipping method to calculate the distribution of background values with the location of all small areas in CCD frames. For crowded star fields, it performs median filtering on the distribution to suppress possible local overestimations due to bright stars (Bertin & Arnouts 1996). Based on the IRAF and SExtractor, a pipeline is built, for data processing, to obtain the instrumental magnitudes that are used widely for NOWT time-domain surveys (Song et al. 2016; Ma et al. 2018; Li et al. 2021).

2.1. Photometric calibration

The standard fields J005945 + 440830 and J234139 + 453900 (Clem & Landolt 2016) were observed during one observing night in order to calculate the instrumental photometry to the standard U, B, V, R, I photometric system. Our $UBVRI$ data were calibrated through about 69 standard stars in Clem & Landolt (2016) field J005945 + 440830. It is generally believed that the atmospheric extinction coefficient of the same site remains basically stable within a certain time interval, so for them, we assumed the typical values for the Nanshan site (Bai et al. 2020). The resulting transformation equations are:

$$\begin{aligned} u &= U + (4.820 \pm 0.023) + (0.590 \pm 0.022) \times X + \\ &\quad (-0.156 \pm 0.061) \times (U - B) \\ b &= B + (1.810 \pm 0.017) + (0.431 \pm 0.029) \times X + \\ &\quad (-0.066 \pm 0.021) \times (B - V) \\ v &= V + (2.107 \pm 0.012) + (0.282 \pm 0.026) \times X + \\ &\quad (0.125 \pm 0.016) \times (B - V) \\ r &= R + (2.125 \pm 0.015) + (0.217 \pm 0.019) \times X + \\ &\quad (0.238 \pm 0.031) \times (V - I) \\ i &= I + (3.210 \pm 0.011) + (0.156 \pm 0.021) \times X + \\ &\quad (-0.022 \pm 0.014) \times (V - I), \end{aligned} \quad (1)$$

where u, b, v, r, i represent the instrumental magnitudes, U, B, V, R, I stand for the magnitudes in the standard system, X is for the airmass, and the remaining two terms are the constant and the color.

According to the transformation Equation 1 and the observation of the standard field J234139 + 453900, we calcu-

¹ Image Reduction and Analysis Facility, is distributed by the National Optical Astronomy Observatory, which is operated by the Association of Universities for Research in Astronomy, Inc., under cooperative agreement with the National Science Foundation. <https://iraf-community.github.io/>

² SExtractor, <https://www.astromatic.net/software/sextractor/> (Bertin & Arnouts 1996).

Table 1. Log of observations of NGC 2355 and its adjacent sky region run in *V* band.

Date	CCD	FOV	Length	Frames	Exposure Time
(yyyy/mm/dd)	(pixel ²)	(arcmin ²)	(h)	(<i>V</i> band)	(s)
2018 Jan 08	4160 × 4136	78 × 78	8	369	35
2018 Jan 09	4160 × 4136	78 × 78	8	360	35
2018 Jan 10	4160 × 4136	78 × 78	8	308	35
2020 Dec 10	4160 × 4136	78 × 78	7	202	30
2020 Dec 11	4160 × 4136	78 × 78	8	358	30
2020 Dec 12	4160 × 4136	78 × 78	8	341	30
2020 Dec 13	4160 × 4136	78 × 78	8	357	30
2020 Dec 14	4160 × 4136	78 × 78	8	354	30
2020 Dec 15	4160 × 4136	78 × 78	5	105	30
2020 Dec 16	4160 × 4136	78 × 78	3	81	30
2020 Dec 17	4160 × 4136	78 × 78	3	92	30
2020 Dec 18	4160 × 4136	78 × 78	2	69	30
2020 Dec 19	4160 × 4136	78 × 78	2	68	30

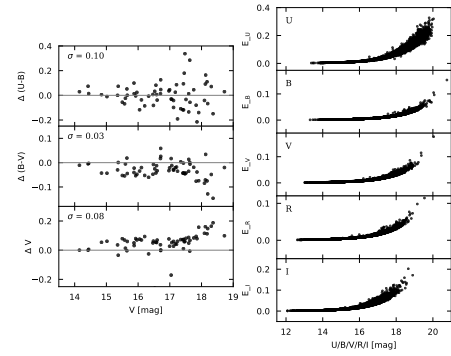
Table 2. *UBVRI* multi-color photometric observation of NGC 2355 and two standard star fields in 2018 January 9.

Target	<i>U</i>	<i>B</i>	<i>V</i>	<i>R</i>	<i>I</i>
J005945+440830	240(s) × 3	90(s) × 3	60(s) × 3	50(s) × 3	80(s) × 3
J234139+453900	240(s) × 3	90(s) × 3	60(s) × 3	50(s) × 3	80(s) × 3
NGC 2355	240(s) × 3	90(s) × 3	60(s) × 3	50(s) × 3	80(s) × 3

late the *UBVRI* standard magnitudes for stars in the standard field J234139 + 453900 to assess the overall quality of the calibrated magnitudes and colors. By cross-correlating with the standard magnitudes of Clem & Landolt (2016), a total of 65 standard stars are found in common. The comparisons of *V* magnitudes, (*U* − *B*) and (*B* − *V*) colors between these two catalogues are shown in the left panels of Figure 1. As illustrated, the final standard deviations are 0.08, 0.03, 0.1 in *V*, (*B* − *V*), and (*U* − *B*), respectively. This indicates that our *V*, (*B* − *V*), and (*U* − *B*) measurements are in fair agreement with those given in Clem & Landolt (2016). We present the photometric error derived from photometric reduction plotted against its corresponding *U*, *B*, *V*, *R*, and *I* magnitudes in the right panels of Figure 1.

2.2. Variable star Detection

For the light curves of the stars observed in the field of view, we use the SysRem algorithm for systematic error subtraction (Tamuz et al. 2005; Ofir et al. 2010). The clouds passing through the field of view will affect the flux measurement of some stars and the observation effect changes over

**Figure 1.** Left panels: Comparisons of the photometry presented in this study with that of Clem & Landolt (2016) for field J234139 + 453900 in *V* magnitudes and (*U* − *B*) − (*B* − *V*) colors. Right panels: Photometric errors against its corresponding *U*, *B*, *V*, *R*, and *I* magnitudes on the standard system from top to bottom.

time, so least-squares fitting is employed to perform a coarse initial decorrelation. Least-squares fitting for the initial zero-point correction is necessary for a better variables searching during the time-domain observations. The detrending algorithm SysRem is employed to eliminate systematic effects hidden in a large set of photometric light curves. Nevertheless, there are additional variances remaining in the corrected data set. Then we use the Gaussian Mixed Model estimation method to determine additional variances in the data set after correction (Gao 2020; Luo et al. 2022). After several repeated iterations of the algorithm, we can get the different light curves of all the stars in the field of view. By visual inspection, we can obtain a number of variable star candidates easily, which can then be analyzed in detail later.

The differential magnitude of each star is given by Collier Cameron et al. (2006) as:

$$x_{ij} = m_{ij} - \hat{m}_j - \hat{z}_i, \quad (2)$$

where m_{ij} is a two-dimensional array of instrumental magnitude, the index i denotes a single CCD frame while the entire seasons' data, the second index j labels an individual star. \hat{m}_j is the mean instrument magnitude for each numbered star and \hat{z}_i is the zero-point correction for each CCD frame. After repeated iterations, the differential light curves of the stars in the field of view are obtained.

The software PERIOD04 (Lenz & Breger 2005) is employed to analyze the period of variable stars. The rectified light curve was fitted with the following formula:

$$m = m_0 + \sum_{i=1}^n A_i \sin(2\pi(f_i t + \phi_i)), \quad (3)$$

where m_0 , A_i , f_i , and ϕ_i are zero-point, amplitude, frequency, and the corresponding phase, respectively.

This software adopts single-frequency Fourier and multi-frequency nonlinear least-squares fitting algorithms. It offers tools to extract the individual frequencies from the multi-periodic content of time series and provides a flexible interface to perform multiple-frequency fits (Lenz & Breger 2005). The frequencies of the intrinsic and statistically significant peaks in the Fourier spectra can be extracted via iterative pre-whitening. The frequency investigations were stopped when the signal-to-noise (S/N) value is less than 4.0 (Breger et al. 1993). Amplitude spectra are computed after pre-whitening. The amplitude spectra of these stars are regarded as another criterion for finding variable stars. In our study, to determine the type of each variable star exactly, we use the main frequency with the highest signal-to-noise ratio extracted from the PERIOD04 to obtain the period of the pulsating variable star as a reference.

2.3. Gaia and LAMOST Data

To identify the variable member stars for NGC 2355, we use the member catalogue of open clusters (Cantat-Gaudin et al. 2018), which provides the combined spatio-kinematic-photometric membership of 1229 open clusters based on the membership assignment code Unsupervised Photometric Membership Assignment in Stellar Clusters (UPMASK) method (Krone-Martins & Moitinho 2014) applied on the Gaia DR2 (Evans et al. 2018). They identified 328 members of the open cluster NGC 2355. Considering the precision of the data, the sources they used are $G < 18$ mag. The membership probabilities of these stars were obtained after 10 iterations of UPMASK, and the membership probability of a star corresponds to the frequency with which it was considered as a member by UPMASK (Krone-Martins & Moitinho 2014). To get the cluster memberships for detected variable stars, we match the equatorial coordinates of more than

30,000 stars we observed with that of the 328 reported members within $1''$. As a result, all of the cluster members with V band photometric data are detected in our field of view.

Large Sky Area Multi-Object Fiber Spectroscopic Telescope (LAMOST) low-resolution spectra have a resolution $R \sim 1800$ and cover the wavelength range 370 – 900 nm (Cui et al. 2012). The spectral data released by LAMOST are selected based on the signal-to-noise ratio (S/N), generally those with $S/N \geq 15$ for bright night and $S/N \geq 6$ for dark night are selected, and those that do not meet the requirements are eliminated. These spectral data that satisfy the requirements are used to obtain the stellar atmospheric parameters for AFGK-type stars (Luo et al. 2015). The seventh data release of LAMOST Galactic Survey (LMOST DR7) has released in 2021, which contains more than 10 million stellar spectra (Zhao et al. 2012). With the importance of stellar parameters (e.g. T_{eff}) of determining variable star types, we cross-match with the low-resolution spectra catalogues of LAMOST DR7 to add extra information to the variable stars, aiming to make our variable star classification more comprehensive.

3. VARIABLE STARS

Relating to the methods mentioned in Section 2, we first use visual inspection to identify variable stars such as eclipsing binaries and long-term variable stars, which can be directly distinguished. Others can be considered as variable stars when their light curves show significant periodic inherent changes in V bands. In our work, we detect 88 variable stars totally, we cross-match them with LAMOST DR7 and we can know that 22 of them have spectral data, and we extract their temperatures as a reference. The information of periods, amplitudes, the shapes of phased light curves, and effective temperatures are taken to classify their types. As a result, we have identified 26 eclipsing binaries, 52 pulsators, 4 rotating variable stars, and 6 unclear type variables during the 88 variables. And Figure 2 present the color-magnitude diagram (CMD) for these variable stars and the stars in the observed field. We then compare our classifications with other surveys, i.e., The All-Sky Automated Survey for Supernovae (ASAS-SN³) and The International Variable Star Index (VSX⁴). As stated by Jayasinghe et al. (2018) in the ASAS-SN survey description, the VSX catalogue seems to be the most comprehensive star catalogue of investigated variable stars in modern era, and includes many kinds of variable stars that detected by a great deal of optical surveys. Therefore, we matched 16 known variable stars that had been determined

³ <https://www.aavso.org/vsx/>

⁴ <https://asas-sn.osu.edu/variables/>

and studied mainly by Jayasinghe et al. (2018), Chen et al. (2018) and Chen et al. (2020).

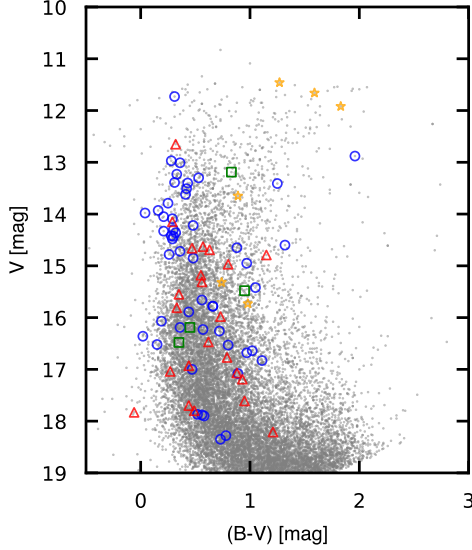


Figure 2. Color-magnitude diagram for the observation filed with variables. The red, blue, green and orange symbols mark the eclipsing binaries, pulsators, rotating variables and unclear variable stars, respectively.

3.1. Eclipsing Binaries

We have detected 26 eclipsing binaries, the details are presented in Table 3. For the amplitudes of these eclipsing binaries, we use PERIOD04 to obtain the periods of them for phase folding firstly, and then sort the phase data in the order from 0 to 1. Secondly, the mathematical method of moving average (Shan et al. 2022) is employed to average the sorted data by taking 20 data in order from the first data. Finally, the amplitude of each eclipsing binary is obtained by subtracting the minimum value from the maximum value obtained. There are 11 EW-type (J1 - J11), 6 EB-type (J12 - J17), and 9 EA-type (J18 - J26) eclipsing binaries, whose types are qualified and classified by us using information such as the light curve patterns, periods, amplitudes, etc. After matching with the VSX and ASAS-SN catalogues, we find that 10 eclipsing binaries have been researched and classified by other studies (Jayasinghe et al. 2018; Chen et al. 2018, 2020), and also find that there is no particular classification standard for the EA and EB type eclipsing binaries. Because the VSX catalogue includes variables discovered by a large number of surveys, some of EB-type binaries found in our work have been matched to the VSX catalogue, and we find that they were not only found in one survey and were determined to be of type EA or EB. Of course, these surveys also include the ASAS-SN survey. The eclipsing binaries that we have determined

to be of type EB are consistent with the variable type given by ASAS-SN, so we have chosen the ASAS-SN determination criteria as a reference. Based on the work mentioned above, these remaining 16 are our newly discovered eclipsing binaries, which contain 7 EW, 2 EB, and 7 EA types. Among the 13 nights observations, we have detected some long-period eclipsing binaries, in which the longest – J18 – is up to about 7.2 days. However, due to night-time observations only, for some eclipsing binaries (J20, J22, J23, J26), our data cannot complete the phase diagram. Therefore, we have identified them as EA-type candidates except for those whose types have been determined by predecessors and can be identified by our visual method. The phase-folded light curve diagrams of all these eclipsing binaries are shown in Figure 3. In addition, we have matched these eclipsing binaries with the open cluster NGC 2355 members determined by Cantat-Gaudin et al. (2018) using *Gaia* DR2, and obtained that 2 eclipsing binaries are the members of this cluster, one is an EW-type, and another is an EA-type eclipsing binary.

On account of cross-match with other studies, Chen et al. (2018) identified variable J9 as an RR Lyrae variable in their study, they determined the period to 0.3319368 d, while we consider it as an eclipsing binary with the period of 0.664248285 d. From Figure 4 we can see that, the period given by Chen et al. (2018) to determine it as an RR Lyrae variable is approximately half of the period given by our determination of it as an EW-type eclipsing binary, and then we used the period given by Chen et al. (2018) to phase collapse our data to obtain the comparison plot in the right panel of Figure 4. It's obvious to see that there is a gap between the primary and secondary maximum of the light curve. Moreover, the light curve of J9 does not conform to the sharp brightening and slow dimming nature of the RR Lyrae variable stars. Thus, we can determine that the variable J9 is an EW-type eclipsing binary with two components sharing a common Losch geometry envelope but with different temperatures based on the unequal height of its primary and secondary minimum moment.

3.2. Pulsating Stars

Except for the eclipsing binaries mentioned above, we also find other 52 pulsating variable stars with significant light curve variations. Referring to Dupret et al. (2005) and Dupret et al. (2005), Aerts et al. (2010) provided an approximate range of period, amplitude, and effective temperature for different types of pulsating stars, which we can use to give a detailed classification of pulsating variable stars in relation to their light curve properties (Uytterhoeven et al. 2011). To make a more accurate determination of the variable star types, we obtain some information especially effective temperature by matching the coordinates of these pulsating variable stars with LAMOST DR7. Since most pulsating variable

Table 3. Specific information on eclipsing binaries in our observation.

ID	RA.	DEC.	V	P	A	T_{eff}	Type	Mem.	Reference
	(degree)	(degree)	(mag)	(d)	(mag)	(K)			
J1	108.7050954	13.7474155	14.63	0.704925149	0.31(1)	—	EW	no	ASAS-SN
J2	108.7378616	13.2368872	17.89	0.362369812	0.4(1)	—	EW	no	our
J3	109.8472352	13.6061456	18.24	0.31797351	0.7(2)	—	EW	no	our
J4	109.6147422	13.5698564	17.61	0.294312087	0.32(9)	—	EW	no	our
J5	109.502782	13.4805083	17.07	1.568406718	0.21(4)	—	EW	no	our
J6	109.4167725	13.7953294	16.77	0.696408296	0.11(3)	—	EW	no	our
J7	109.412816	14.3991508	17.7	0.306333395	0.42(6)	5569 ± 82	EW	no	C20
J8	109.3495498	13.7812947	15.18	0.318030478	0.10(3)	—	EW	yes	our
J9	109.2058456	13.7006874	14.97	0.664248285	0.54(1)	6981 ± 37	EW	no	C18
J10	109.1749339	14.0861158	15.98	0.283403222	0.17(4)	—	EW	no	C20
J11	109.0838882	13.7072543	16.47	0.343961735	0.24(4)	—	EW	no	our
J12	109.8432496	14.268068	14.79	0.290520284	0.54(1)	4050 ± 50	EB	no	C20
J13	109.6709524	14.3419885	17.83	0.532057738	0.7(1)	—	EB	no	our
J14	109.4418925	14.2416662	15.81	0.575876016	0.54(3)	—	EB	no	ASAS-SN
J15	109.3781482	13.5799012	11.06	0.658875512	0.255(8)	6406 ± 21	EB	no	ASAS-SN
J16	109.0725927	13.696204	15.31	0.502755629	0.61(2)	—	EB	no	our
J17	109.0658004	13.8280396	12.65	0.581627848	0.613(8)	—	EB	no	ASAS-SN
J18	109.6309312	13.9601402	15.55	7.206777787	1.40(6)	—	EA	no	ASAS-SN
J19	109.454682	14.3508626	17.80	0.549391707	1.0(3)	—	EA	no	our
J20	109.2499035	14.2216055	18.21	3.024331909	0.5(2)	—	EA	no	our
J21	109.1642519	13.8676077	17.19	0.913374903	0.80(8)	—	EA	yes	our
J22	109.1448447	13.7156306	14.69	1.545501416	0.11(1)	6064 ± 24	EA	no	our
J23	109.0751204	14.0879028	14.66	2.562004676	0.18(2)	—	EA	no	our
J24	109.0422302	13.8363867	14.15	3.4220256	0.84(2)	—	EA	no	ASAS-SN
J25	108.9081585	13.6208906	17.04	0.797580838	0.59(5)	—	EA	no	our
J26	108.8794118	14.0339731	16.93	3.44607673	0.30(4)	—	EA	no	our

NOTE—Column 1: variable stars' ID. Column 2 and 3: right ascension and declination (J2000). Column 4: the magnitude of variable stars in V band. Column 5: the main period of variable stars. Column 6: the amplitude of folded light curves calculated by PERIOD04. Column 7: relatively accurate effective temperature from LAMOST DR7. Column 8: different types of variable stars. Column 9: membership of variable stars provided by [Cantat-Gaudin et al. \(2018\)](#). Column 10: reference of variables detection. ASAS-SN, C18 and C20 indicate that the variables were found by [Jayasinghe et al. \(2018\)](#), [Chen et al. \(2018\)](#) and [Chen et al. \(2020\)](#), respectively.

stars have multi-mode pulsation modes, we calculated the fundamental and harmonic frequencies of each pulsating star using Period04 ([Lenz & Breger 2005](#)). There is also a distinction between fundamental and harmonic frequencies of pulsating variable stars, and we generally take the frequency with the highest signal-to-noise ratio as the fundamental frequency to calculate the main period of the pulsating variable star as its intrinsic period. To verify the accuracy of all the pulsating stars' primary frequencies, then we performed fundamental frequency analyses for all time-series data in V band by using the Lomb-Scargle periodogram ([VanderPlas & Ivezić 2015](#)) of the Astropy package ([Astropy Collaboration et al. 2013, 2018](#)). The results are shown in Figure 5, and

both of them have relatively good agreement. All of their information is listed in Table 4. Using these main periods extracted from fundamental frequencies, we show the phase folding diagrams of these 52 pulsating variable stars in Figures 6 and 7.

Finally, we have classified these 52 pulsating variable stars into different types: 38 δ Scuti (Y1 - Y38), 3 γ Dor (Y39 - Y41), 9 RR Lyrae variable stars (Y42 - Y50), and 2 Cepheid I type variable stars (Y51 - Y52). As for these 9 RR variable stars, we also classify them specifically into R Rab and RRc types pulsating variable stars according to their periods, amplitudes, the morphology of their light curves and so on. Furthermore, by comparing the bulk light curves, we find

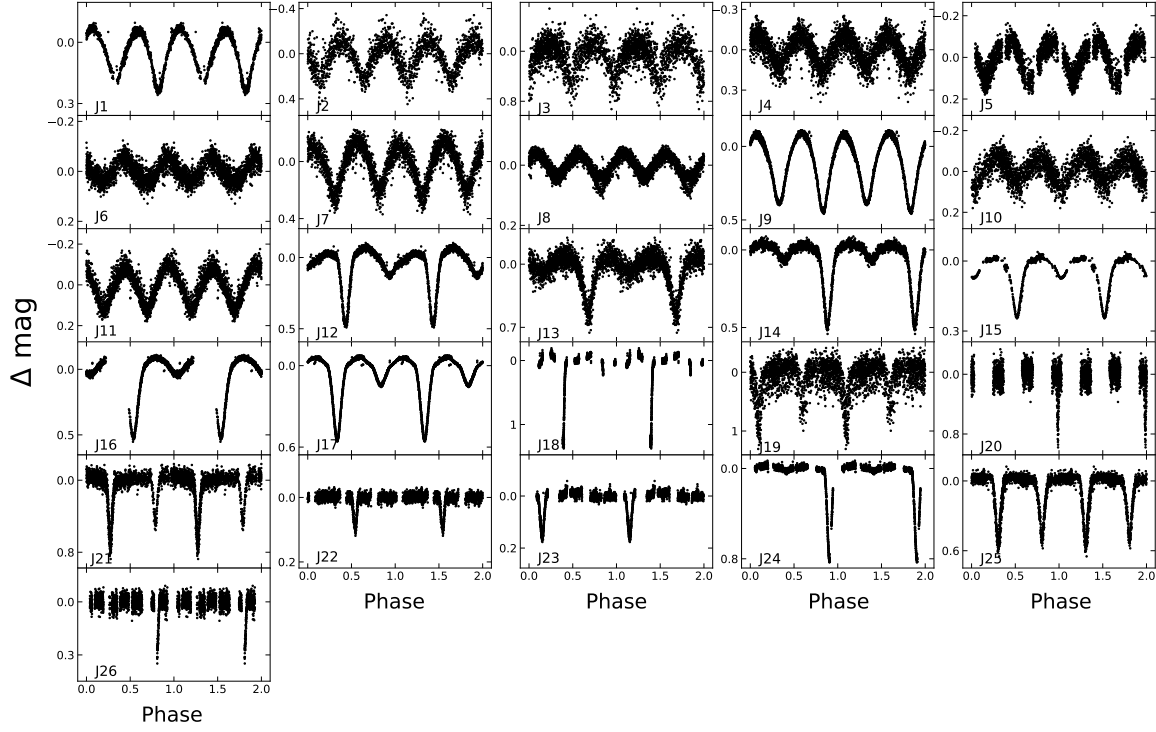


Figure 3. The phase-folded light curves for these 26 eclipsing binaries.

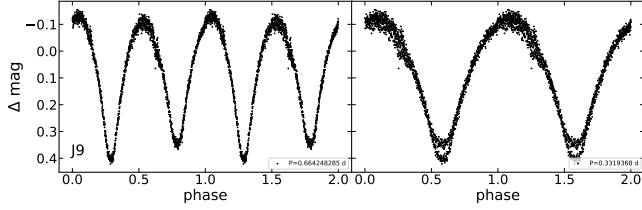


Figure 4. The different phase-folded light curves for J9. left panel: the light curve of J9 with the period given by us. Right panel: the light curve with the period given by [Chen et al. \(2018\)](#) based on our observation data.

that some of them are worth further studying. For instance, a high amplitude δ Scuti (HADS) among the 38 δ Scuti variable stars and the 3 γ Dor we determined, which can be used to study the different modes of radial and non-radial modal pulsations in stellar evolution ([Breger 2000](#)). Meanwhile, classical Cepheids are the most important and accurate distance indicators for us to establish astronomical distance scales ([Chen et al. 2018](#)). RR Lyrae constitutes another useful distance indicator for tracking ancient environments of the structure of Milky Way ([Drake et al. 2013](#); [Gran et al. 2016](#)), as well as the neighborhood of the solar system ([Layden 1998](#)). These two types of variable stars have also been identified in our work. For the pulsating variable stars, we have done the same catalog matching for VSX and ASAS-SN as for the preceding eclipsing binaries, finding that only

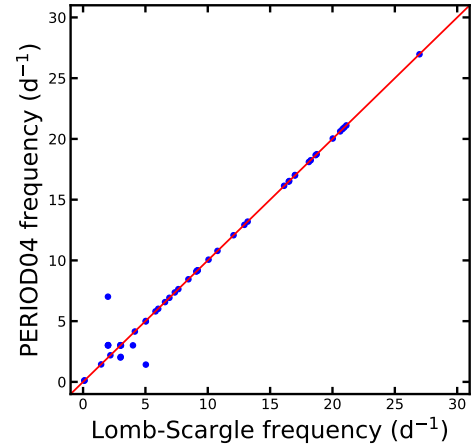


Figure 5. Comparison of PERIOD04 and Lomb-Scargle extracted pulsating variable star frequencies.

3 of the pulsating stars (Y21, Y38, Y44) in our list were identified as variables in ASAS-SN and our results are consistent with theirs ([Jayasinghe et al. 2018](#)). We have done a member star match for these pulsating variable stars as well, similar to the previous Subsection 3.1, and eventually matched 9 members with the catalogue of [Cantat-Gaudin et al. \(2018\)](#). All of

the 9 pulsating star members of the open cluster NGC 2355 are δ Scuti pulsating variables.

3.3. Rotating Variables

In the classification of pulsating variable stars given by Aerts et al. (2010), there is another category of periodic variable stars that cannot be classified based on their amplitudes, periods, temperatures, and light curves. The detailed parameters of these 4 variables with other categories are listed in Table 5 and their phase diagrams are shown in the later order of Figure 7.

Therefore, we first match these 4 variable stars presenting two peaks of different heights with the VSX and ASAS-SN star catalogues, finding that 2 stars were determined to be of the variable star by previous studies, one (WH2) being a BY Draconis-type variable star (Chen et al. 2020), while another (WH4) being a ROT-type variable star (Jayasinghe et al. 2018). BY Draconis-type variable stars with periods from a pinch of 1 to 120 days and amplitudes from several hundredths to 0.5 mag in V band, are emission-line dwarfs of the dKe-dMe spectral type exhibiting quasi-periodic light variations. The variation of light is caused by the axial rotation of the star with varying degrees of the unevenness of surface brightness, spots or chromospheric activity (Chen et al. 2020). The ROT-type variable is classified by Jayasinghe et al. (2018) due to their light curves showing evidence of rotational modulation. It differs from the above 3 BY Draconis-type stars in the morphology of the light curves, which may be due to the periastron material accompanying the rotation of the star.

Since the remaining two variable stars (WH1, WH3) show similar morphology to WH2 in terms of light transitions, we tentatively conclude that both of them are also BY Draconis-type variable stars. Given that they are both caused by star rotation regardless of whether they are BY Draconis-type or ROT-type variable stars, we call this class of variable stars rotating variable stars. The light variation of the pulsating variable stars is mainly due to their endogenous causes, while the light change of the rotating variables is due to their own rotation accompanied by spots, flares, periastron matter, etc. The 4 rotational variable stars (WH1 - WH4) have light curves that are due to their own rotation, which can be caused either by the star brightness or spots on their surface or by the peri-stellar material around the stars rotating with them.

3.4. Unclear Variable Stars

In addition to the periodic variables, we also detected 6 non-periodic variable stars (N1 - N6). It is difficult to classify these non-periodic stars only based on their light curves, so we list some of the parameters that can be obtained for these unclear variable stars as much as possible in Table 6. The period of these unknown variable stars is relatively long,

thus preventing us from obtaining the complete light curves of these long-period variable stars due to only a few days of observation data. From Figure 8 we can see that they show photometric variability, but owing to the variety of variable stars and their inability to achieve all conditions that exactly match the period, amplitude, and effective temperature information of a particular class of variable stars, and we tentatively classify them as unclear variable stars.

By matching with the VSX and ASAS-SN catalogues, we obtained the type of one of the unclear variable stars, N5, which is an SR-type variable given by ASAS (Jayasinghe et al. 2018) with a period of up to about 465 days, a level we cannot reach with our short-term time-domain survey. The full name of the SR variable stars is Semi-Regular variable stars, which are cool giant evolved stars on the asymptotic giant branch. These are stars at the end of their lives, greatly expanded from birth, with very long pulsation periods, ranging from 10 to 1000 days. SR-type variables exhibit periodic variations, with interruptions in their pulsation periods leading to irregularities in their light curves. A large fraction of semi-periodic variable stars has two distinct modes of variability, which have long secondary periods superimposed on the shorter period variability (Jayasinghe et al. 2018). At a later stage, we put these unclear variable stars together to study them as well, intending to find whether they belong to variable stars that are not identified as members of the open cluster NGC 2355.

4. DISCUSSION

Overall, additional work has been done on the open cluster NGC 2355 combined with the work of predecessors. Employing *Gaia* data, we have analyzed the nature of cluster variable member stars and obtained possible cluster member variable stars through a series of analyses. At the same time, based on the previous work done for this cluster, we have also refined the cluster parameters in conjunction with our work.

4.1. Membership of Variable Stars

We cross-matched our variable stars with the member catalogue of NGC 2355 reported by Cantat-Gaudin et al. (2018) which contains 328 members to check the membership of variable stars. 11 variable stars were included in the cluster members, including 2 eclipsing binaries and 9 pulsating variables. In Figure 9, we show the homogeneity of these variable cluster members in the spatial, proper motion, and parallax.

Just as Tarricq et al. (2021) pointed out that the members provided by Cantat-Gaudin et al. (2018) were mainly focused on the inner parts of the clusters and unable to provide members in the peripheral regions of open clusters. Combined with proper motion and parallax data from *Gaia* DR2 (Lindgren et al. 2018) and the members of Cantat-Gaudin et al.

Table 4. Detailed information on pulsating stars in our observation.

ID	RA.	DEC.	V_{mag}	P	A	T_{eff}	Type	Mem.	Reference
	(degree)	(degree)	(mag)	(d)	(mag)	(K)			
Y1	109.9108557	13.7159228	15.89	0.331521548	0.054(2)	—	δ Scuti	no	our
Y2	109.8728109	14.0712854	14.48	0.058868469	0.0205(2)	7418 ± 44	δ Scuti	no	our
Y3	109.8470245	14.3053479	15.42	0.144456746	0.0181(4)	—	δ Scuti	no	our
Y4	109.768027	14.0796784	16.68	0.142582429	0.063(3)	—	δ Scuti	no	our
Y5	109.7150925	13.5388977	17.90	0.166207444	0.073(4)	—	δ Scuti	no	our
Y6	109.5935811	13.744437	14.72	0.082845863	0.0085(4)	—	δ Scuti	no	our
Y7	109.5237211	14.0054341	12.97	0.060482395	0.0042(2)	—	δ Scuti	no	our
Y8	109.5186289	13.8422864	15.66	0.331221714	0.0160(6)	—	δ Scuti	no	our
Y9	109.5036782	13.7302877	16.64	0.33123391	0.080(1)	—	δ Scuti	no	our
Y10	109.4982053	13.80885	14.33	0.048050167	0.0039(2)	—	δ Scuti	candidate	our
Y11	109.5012411	14.0079472	13.62	0.049919365	0.0032(2)	—	δ Scuti	candidate	our
Y12	109.4411585	13.7474767	16.36	0.241134804	0.0397(7)	—	δ Scuti	no	our
Y13	109.3908596	14.0971415	14.60	0.152285134	0.0219(8)	—	δ Scuti	no	our
Y14	109.3186704	13.8888941	14.30	0.054809912	0.0043(2)	7292 ± 33	δ Scuti	yes	our
Y15	109.3142335	13.7722935	14.22	0.053576176	0.0135(3)	—	δ Scuti	yes	our
Y16	109.2418059	13.768747	12.88	0.075796607	0.0035(1)	—	δ Scuti	yes	our
Y17	109.2872054	14.2818177	14.78	0.109619824	0.0145(4)	7149 ± 30	δ Scuti	no	our
Y18	109.2700543	14.0465042	16.23	0.172303837	0.0337(7)	—	δ Scuti	no	our
Y19	109.2186735	13.760371	13.3	0.130980433	0.0073(2)	—	δ Scuti	yes	our
Y20	109.2324957	13.9456429	13.39	0.060662342	0.0082(3)	7374 ± 17	δ Scuti	yes	our
Y21	109.2154808	13.9060147	13.01	0.110080136	0.0266(5)	7287 ± 17	δ Scuti	no	ASAS-SN
Y22	109.2077096	13.7325699	13.98	0.061953548	0.0093(2)	—	δ Scuti	yes	our
Y23	109.2169443	13.6855261	14.43	0.053359577	0.0170(3)	—	δ Scuti	yes	our
Y24	109.2148984	14.3025137	16.07	0.047762516	0.0175(5)	7315 ± 219	δ Scuti	no	our
Y25	109.1399024	14.0107299	16.52	0.037081897	0.029(1)	—	δ Scuti	no	our
Y26	109.1111801	13.8594634	14.05	0.058717766	0.0031(2)	—	δ Scuti	yes	our
Y27	109.0953706	13.4844115	15.78	0.109163347	0.0147(5)	5941 ± 119	δ Scuti	no	our
Y28	109.0953684	13.4844122	15.78	0.109163347	0.0148(4)	5941 ± 119	δ Scuti	no	our
Y29	109.0793748	13.4891903	13.41	0.330042421	0.0042(2)	—	δ Scuti	no	our
Y30	109.080247	13.9584684	14.09	0.047367988	0.0037(2)	—	δ Scuti	candidate	our
Y31	109.0186492	13.4600758	11.73	0.055242417	0.0066(3)	7249 ± 189	δ Scuti	no	our
Y32	108.9851145	13.4064989	17.87	0.135827969	0.063(2)	—	δ Scuti	no	our
Y33	108.9608518	13.5199721	13.40	0.099382485	0.0106(2)	7218 ± 34	δ Scuti	no	our
Y34	108.9209026	13.5424117	13.51	0.108904205	0.0038(2)	—	δ Scuti	no	our
Y35	108.8926011	13.7851013	13.23	0.09272541	0.0093(2)	7219 ± 15	δ Scuti	candidate	our
Y36	108.8190455	13.470833	14.95	0.118382592	0.0219(3)	—	δ Scuti	no	our
Y37	109.2025478	13.7603428	13.79	0.04849899	0.0073(3)	7418 ± 58	δ Scuti	yes	our
Y38	109.5389492	14.0900076	13.93	0.077362389	0.2005(8)	—	HADT	no	ASAS-SN
Y39	108.6997067	14.1040814	14.42	0.333430555	0.0280(4)	7032 ± 30	γ Dor	no	our
Y40	109.6759171	13.2210089	14.85	0.703078873	0.0114(3)	7071 ± 30	γ Dor	no	our
Y41	109.513806	13.474619	16.53	0.695089343	0.0570(9)	—	γ Dor	no	our
Y42	109.703044	13.9135448	18.28	0.498651049	0.245(6)	—	RRab	no	our
Y43	109.4809065	13.7855212	17.08	0.485694946	0.19(1)	—	RRab	no	our
Y44	109.4685443	14.3504307	14.36	0.456430404	0.475(5)	6385 ± 31	RRab	no	ASAS-SN
Y45	108.7428509	14.0129341	17.00	0.200895398	0.070(2)	—	RRc	no	our
Y46	109.8974297	13.933293	18.35	0.199458274	0.41(1)	—	RRc	no	our
Y47	109.675003	14.3738616	16.83	0.333775517	0.256(7)	—	RRc	no	our
Y48	109.5392842	14.3699187	17.88	0.332466859	0.142(4)	—	RRc	no	our
Y49	109.3758993	13.4016689	16.94	0.331063381	0.130(4)	—	RRc	no	our
Y50	109.3098908	13.8720478	16.19	0.332434033	0.087(2)	—	RRc	no	our
Y51	109.5133375	14.0605146	16.26	9.658083467	0.0609(9)	—	Cepheid I	no	our
Y52	109.4736844	13.943555	14.65	7.978416787	0.1127(4)	—	Cepheid I	no	our

NOTE—The same information as Table 3 but for pulsating stars.

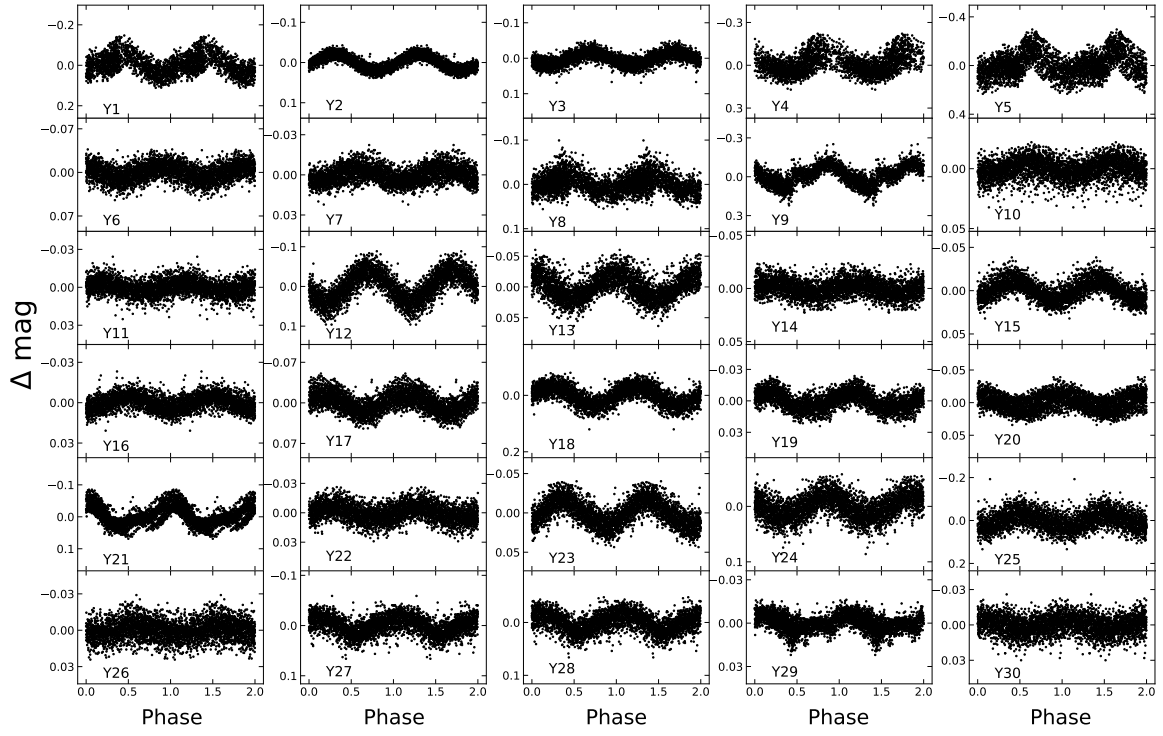


Figure 6. Same as Figure 3, but for pulsating stars of Y1-Y30.

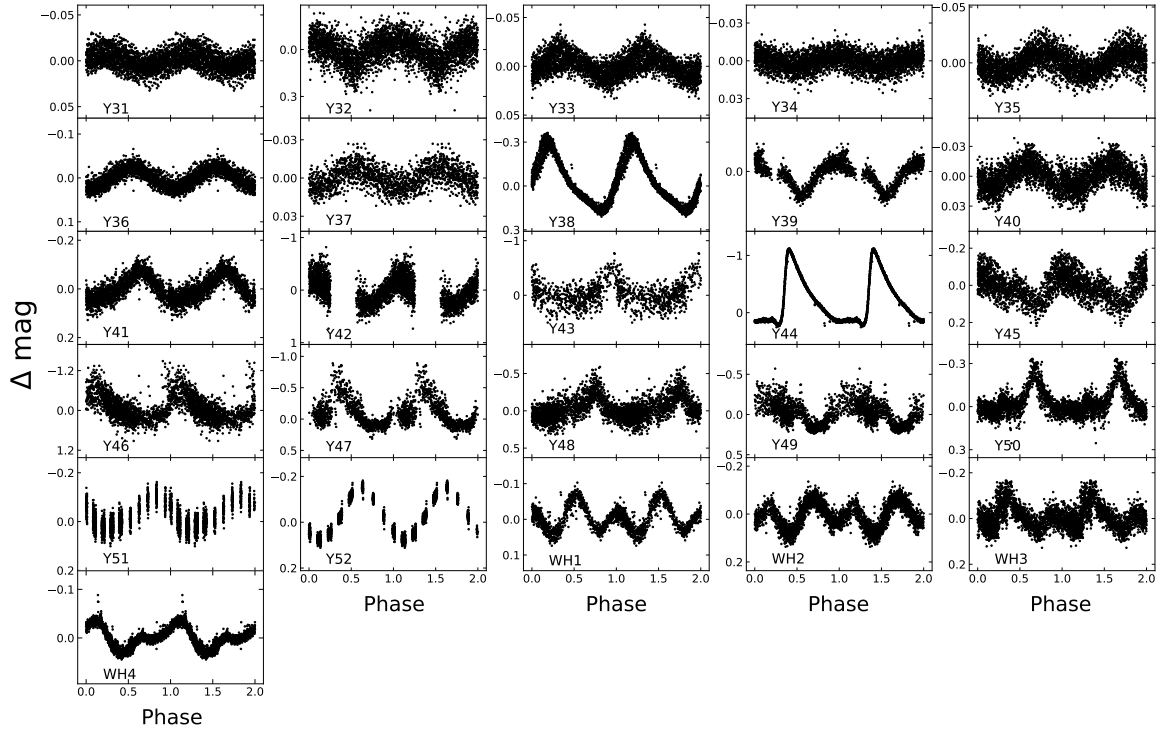


Figure 7. Light curves of pulsating stars Y31-Y42 and other type variables W1-W4.

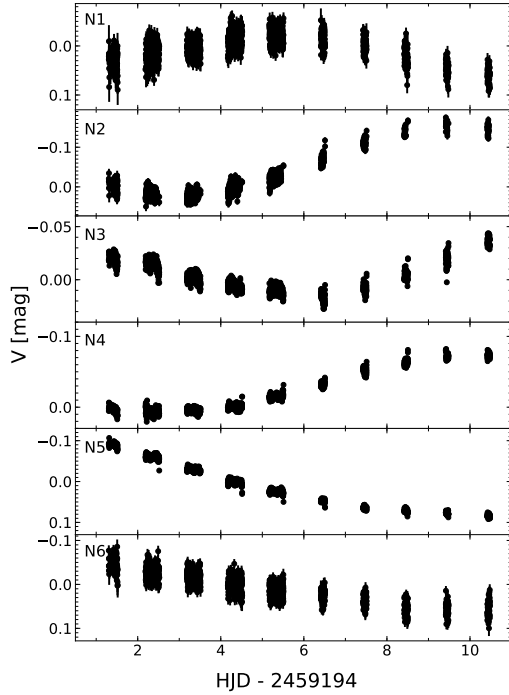
Table 5. Detailed information on rotating variable stars in our observation.

ID	RA.	DEC.	V_{mag}	P	A	T_{eff}	Type	Mem.	Reference
	(degree)	(degree)	(mag)	(d)	(mag)	(K)			
WH1	108.7934201	13.2461453	15.48	0.256759358	0.0379(7)	5000 ± 47	BY	no	our
WH2	109.2705053	13.4954579	16.48	0.524295961	0.0556(9)	—	BY	no	C20
WH3	109.1498495	14.0871941	16.19	0.333037361	0.037(1)	—	BY	no	our
WH4	109.0146283	14.1139968	13.19	0.722455061	0.0238(2)	—	ROT	no	ASAS-SN

NOTE—The same information as Table 3 but for rotating variable stars.

Table 6. Information on unclear variables in our observation.

ID	RA.	DEC.	V_{mag}	P	T_{eff}	Type	Mem.	Reference
	(degree)	(degree)	(mag)	(d)	(K)			
N1	109.6418403	13.5294504	15.32	—	—	unknown	no	our
N2	109.5479767	14.3981865	13.65	—	—	unknown	no	our
N3	109.4011549	13.9683771	11.66	—	—	unknown	no	our
N4	109.3044602	14.1823171	11.46	—	—	unknown	no	our
N5	109.2825841	13.2909009	11.92	464.9215097	—	SR	no	ASAS-SN
N6	109.1929547	13.6178583	15.73	—	4803 ± 57	unknown	no	our

**Figure 8.** The light curves of this 6 long period unclear variable stars which are listed in Table 6.

(2018) in the core region, we reanalyze the membership for variable stars. Figure 9 (a) presents the spatial positions of the member stars of NGC 2355 and the 88 variable stars. The proper motion distributions of variable stars and members are shown in Figure 9 (b). In proper motion space, we set a circular region centered on $(\mu_\alpha, \mu_\delta) = (-3.802, -1.086)$ mas yr⁻¹ with radius 1.5 mas yr⁻¹ as the selection criteria for variable stars. After excluding that located outside the criteria circle, 24 variable stars remain, including 3 eclipsing binaries and 21 pulsating variables.

To further purify the variable members, we apply the parallax criteria to select the variable member candidates from the 24 remaining variables, which are shown in panel (c) of Figure 9. For the parallax distribution of the 328 members of Cantat-Gaudin et al. (2018), a single Gaussian profile can be well fitted, we exclude variable stars with parallax ω greater than $3\sigma_\omega$ of the Gaussian distribution. After this selection, the variable member candidates retain 19 stars, including 3 eclipsing binaries and 16 pulsating variables.

In addition, we also employ proper motion parameters to perform the kinematic analysis for the selection boundaries, as shown in panel (d) of Figure 9. Panel (d) of Figure 9 shows the spatial distributions and corresponding tangential velocities of the remaining 19 variable stars and the cluster members. From the vector distribution of NGC 2355 and variable

stars, it can be seen that 4 pulsating stars (V10, V11, V30, and V35) almost have the same direction and magnitude as that of the cluster members.

We consider that V10, V11, V30, and V35 pulsating stars are very likely to be missing variable members of the cluster, which are located at the peripheral region of NGC 2355. We present them as member star candidates in Table 4.

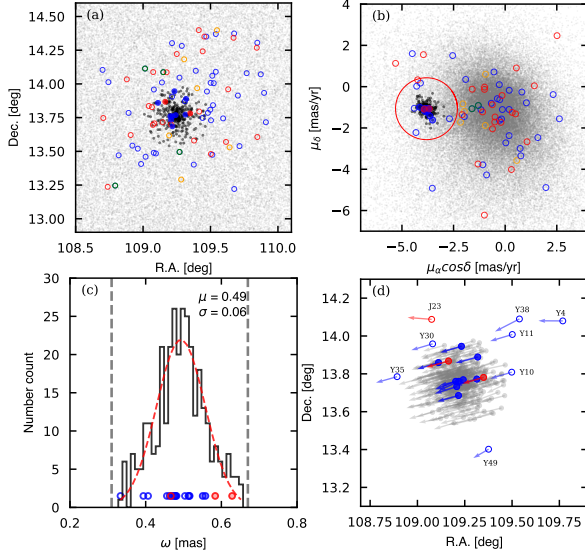


Figure 9. (a): Spatial distribution for the cluster members and 88 variable stars, (α_{J2000} δ_{J2000}). (b): proper motion distribution for them. (c): Histogram of parallax (ω) for cluster members (black line) and variable stars located in the area of $3\sigma_\omega$ boundary (gray dashed lines). The histogram of members' parallax is fitted with a single Gaussian profile (red dashed line). (d): Spatial distribution for the cluster members and circled variable stars in (c) with their tangential velocities. Arrows point out the direction of tangential velocities for each star and arrow length is in proportion to the tangential speed. In top panels, light grey dots mean the complete samples of observation, and black dots represent 328 cluster members. Red, blue, green, and orange circles represent eclipsing binaries, pulsators, rotating variables, and unclear variables, respectively. Solid and hollow refer to whether they are matched members of NGC 2355.

4.2. Stellar Parameters

As we mentioned in the previous Section 2, we not only performed U, B, V, R, I multi-color metering on the standard star field, but also the open cluster NGC 2355. We used the member catalogue of Cantat-Gaudin et al. (2018) to match the cluster members with the stars in the field of view for which multi-color photometry was available and corrected and finally obtained 172 cluster members.

Reddening is one of the important basic parameters of open cluster, which can significantly affect other fundamental parameter determinations. The plots of classic two-color dia-

gram (TCD, $U - B/B - V$) are very useful tools to estimate the reddening. We plotted the $(U - B)$ versus $(B - V)$ diagram in Figure 10 to estimate the reddening of NGC 2355. The intrinsic zero-age main-sequence (ZAMS) from Turner (1976, 1979) is fitted by the reddening slope of $E(U - B)/E(B - V)$ as 0.76. Through fitting ZAMS to the cluster member, we obtained the $E(B - V) = 0.24 \pm 0.06$. The best fitting result is presented in Figure 10.

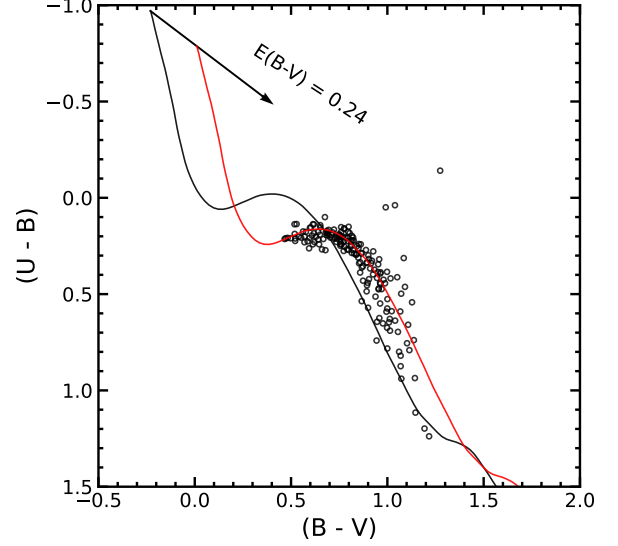


Figure 10. The $(U - B)$ versus $(B - V)$ color-color diagram of the open cluster NGC 2355. The black solid curve line represents the locus of Turner (1976, 1979) ZAMS for solar metallicity. And, the red solid curve line is fitted to the black hollow circle by translating over the ZAMS with the condition given in the text.

The CMD is usually used for the fundamental parameter estimations for open clusters, such as reddening, metallicity, distance, and age. All the 328 members provided by (Cantat-Gaudin et al. 2018) are plotted in the CMD in Figure 11. To transform the observational magnitude G_{mag} and colors ($G_{BP} - G_{RP}$) of each star to the absolute magnitude M_G and intrinsic colors ($G_{BP} - G_{RP}$) (Gaia Collaboration et al. 2018), distance and reddening are needed. We take the distance of 1902^{+447}_{-304} pc estimated from Cantat-Gaudin et al. (2018) for all the members, corresponding the distance modulus about $(m - M) = 11.4$ mag. For the extinction coefficients A_G , $A_{G_{BP}}$, and $A_{G_{RP}}$, we followed the transformation relation for Gaia bands:

$$A_M/A_V = c_{1M} + c_{2M}(G_{BP} - G_{RP}) + c_{3M}(G_{BP} - G_{RP})^2 + c_{4M}(G_{BP} - G_{RP})^3 + c_{5M}A_V + c_{6M}A_V^2 + c_{7M}(G_{BP} - G_{RP})A_V, \quad (4)$$

where M indicates the G , G_{BP} , or G_{RP} band, and $c_{1...7M}$ belong to a set of coefficients defined in Gaia Collaboration et al. (2018) Table 1.

In order to estimate the age of NGC 2355, we adopt the theoretical isochrones from PARSEC (Bressan et al. 2012) stellar evolution models to perform the CMD fitting. For the metallicity, we adopted the parameters provided by the high-resolution spectra of Soubiran et al. (2000), Jacobson et al. (2011) and Donati et al. (2015), and averaged them to obtain a metal value $[\text{Fe}/\text{H}] = -0.07 \pm 0.01$ dex. Using theoretical isochrones of different age (age = 700, 800, 900 and 1000 Myr) with $[\text{Fe}/\text{H}] = -0.07$ dex and $A_V = 0.744$ ($A_V = R_V \times E(B - V)$; $R_V = 3.1$). We adopted Equation (2) in Liu & Pang (2019) to evaluate which of these isochrones shows the best fit. Since the $\bar{d}^2 = 0.0118$ for age = 800 Myr is less than the values $\bar{d}^2 = 0.0120$ and 0.0128 for age = 700 and 900 Myr, we consider 800 ± 50 Myr as the more reliable age for NGC 2355. Figure 11 shows the isochrone fitting result.

Meanwhile, the instability region adopted from Jeffery & Saio (2016) and the 15 variable members and member candidates are also presented in the CMD. It can be seen that all these pulsating star members are located in the instability region, which verifies the reliability of our variable star classification.

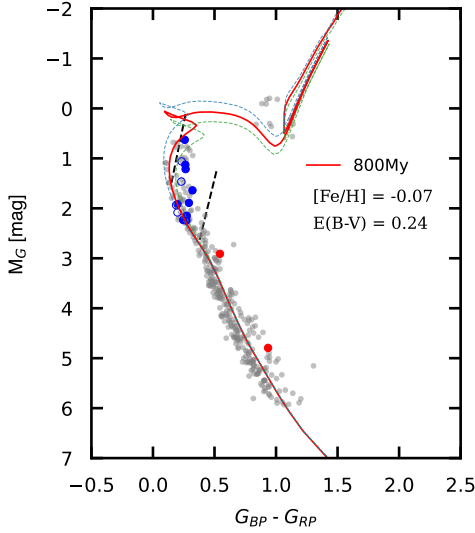


Figure 11. CMD of open cluster NGC 2355 with isochrone and the instability strip of δ Scuti stars. Grey dots represent the 328 member stars of open cluster NGC 2355 by Cantat-Gaudin et al. (2018). The PARSEC isochrones of 700, 800, and 900 Myr with metallicity $[\text{Fe}/\text{H}] = -0.07$ and extinction $A_V = 0.744$ are indicated by the blue dashed, green dashed, and red solid lines, respectively.

The approximate range of theoretical pulsation instability strip on the isochronous line is pointed by two black dashed lines. Different types of member variable stars are plotted with different symbols in the diagram the same as described in Figure 9.

5. SUMMARY

We have investigated and characterized an extensive variability search among stars in the field of the open cluster NGC 2355 and its surrounding field by photometric observations with NOWT. We detected 88 variable stars from 13 nights photometric observations, containing 72 new variable stars and 16 known variables. They are classified into different types according to their main periods, amplitudes, the specific morphology of their light curves, effective temperature, etc. Finally, we discovered 26 eclipsing binaries, including 11 EW-type, 6 EB-type, and 9 EA-type eclipsing binaries. 52 pulsating variable stars are also detected in this work, containing 38 δ Scuti stars which include 1 large-amplitude δ Scuti (HADS), 3 γ Dor variables, 9 RR Lyrae, and 2 Cepheid I type variable stars. Besides, there are also 4 rotational type variable stars because their light variations are caused by rotation, and 6 long-period stars whose types are not clear. For those variable stars for which no type has been determined, we may need more observations later to identify and classify these unknown variable stars.

We also consult the cluster members established by Cantat-Gaudin et al. (2018) and the database of Gaia DR2 to obtain the membership probability and the physical parameters of NGC 2355. 11 variable stars were determined as cluster members by Cantat-Gaudin et al. (2018), including 2 eclipsing binaries and 9 pulsating member stars. In addition to the 11 variable members reported by Cantat-Gaudin et al. (2018), we find 4 new cluster member candidates by detailed analysis. They are confirmed by the homogeneity of the position and kinematics of the star with the identified cluster members. We determined the reddening of NGC 2355 to be $E(B - V) = 0.24$ by TCD, and then combined the average of the metallicity given by previous authors using high-resolution spectra and the distance values given by Cantat-Gaudin et al. (2018) to perform isochrones fitting for different age gradients. The best fit yields $\log(\text{Age}/\text{yr}) = 8.9$, $[\text{Fe}/\text{H}] = -0.07$ dex, $m - M = 11.4$ mag, and $E(B - V) = 0.24$.

ACKNOWLEDGMENTS

We are grateful to an anonymous referee for valuable comments which help to improve the presentation. The authors acknowledge the National Natural Science Foundation of China under grant U2031204 and the science research grants from the China Manned Space Project with NO. CMS-CSST-2021-A08. The CCD photometric data of NGC 2355 were obtained with the Nanshan One-meter Wide-field Telescope of Xinjiang Astronomical Observatory. This work has made use of data from the European Space Agency (ESA) mission Gaia (<https://www.cosmos.esa.int/web/gaia>), processed by the Gaia Data Processing and Analysis Consortium (DPAC, <https://www.cosmos.esa.int/web/gaia/dpac/>).

consortium). The Large Sky Area Multi-Object Fiber Spectroscopic Telescope (LAMOST) is a National Major Scientific Project built by the Chinese Academy of Sciences. Funding for the project has been provided by the National Development and Reform Commission. LAMOST is operated and managed by the National Astronomical Observatories, Chinese Academy of Sciences.

Software: SExtractor (Bertin & Arnouts 1996), PERIOD04 (Lenz & Breger 2005), IRAF (Tody 1986, 1993), astropy (Astropy Collaboration et al. 2013, 2018)

REFERENCES

- Aerts, C., Christensen-Dalsgaard, J., & Kurtz, D. W. 2010, *Asteroseismology*, Astronomy and Astrophysics Library. ISBN 978-1-4020-5178-4. Springer Science+Business Media B.V., 2010, p.
- Ann, H. B., Lee, M. G., Chun, M. Y., et al. 1999, *Journal of Korean Astronomical Society*, 32, 7
- Astropy Collaboration, Robitaille, T. P., Tollerud, E. J., et al. 2013, *A&A*, 558, A33. doi:10.1051/0004-6361/201322068
- Astropy Collaboration, Price-Whelan, A. M., Sipőcz, B. M., et al. 2018, *AJ*, 156, 123. doi:10.3847/1538-3881/aabc4f
- Bai, C.-H., Feng, G.-J., Zhang, X., et al. 2020, *Research in Astronomy and Astrophysics*, 20, 211. doi:10.1088/1674-4527/20/12/211
- Bertin, E. & Arnouts, S. 1996, *A&AS*, 117, 393. doi:10.1051/aas:1996164
- Bessell, M. S. 1990, *PASP*, 102, 1181. doi:10.1086/132749
- Breger, M., Stich, J., Garrido, R., et al. 1993, *A&A*, 271, 482
- Breger, M. 2000, *Delta Scuti and Related Stars*, 210, 3
- Bressan, A., Marigo, P., Girardi, L., et al. 2012, *MNRAS*, 427, 127. doi:10.1111/j.1365-2966.2012.21948.x
- Cantat-Gaudin, T., Jordi, C., Vallenari, A., et al. 2018, *A&A*, 618, A93. doi:10.1051/0004-6361/201833476
- Chen, L., Hou, J. L., & Wang, J. J. 2003, *AJ*, 125, 1397. doi:10.1086/367911
- Chen, X., Wang, S., Deng, L., et al. 2018, *ApJS*, 237, 28. doi:10.3847/1538-4365/aad32b
- Chen, X., Wang, S., Deng, L., et al. 2020, *ApJS*, 249, 18. doi:10.3847/1538-4365/ab9cae
- Clem, J. L. & Landolt, A. U. 2016, *AJ*, 152, 91. doi:10.3847/0004-6256/152/4/91
- Collier Cameron, A., Pollacco, D., Street, R. A., et al. 2006, *MNRAS*, 373, 799. doi:10.1111/j.1365-2966.2006.11074.x
- Cousins, A. W. J. 1976, *Monthly Notes of the Astronomical Society of South Africa*, 35, 70
- Cui, X.-Q., Zhao, Y.-H., Chu, Y.-Q., et al. 2012, *Research in Astronomy and Astrophysics*, 12, 1197. doi:10.1088/1674-4527/12/9/003
- Donati, P., Bragaglia, A., Carretta, E., et al. 2015, *MNRAS*, 453, 4185. doi:10.1093/mnras/stv1914
- Drake, A. J., Catelan, M., Djorgovski, S. G., et al. 2013, *ApJ*, 763, 32. doi:10.1088/0004-637X/763/1/32
- Dupret, M.-A., Grigahcène, A., Garrido, R., et al. 2005, *MNRAS*, 360, 1143. doi:10.1111/j.1365-2966.2005.09114.x
- Dupret, M.-A., Grigahcène, A., Garrido, R., et al. 2005, *A&A*, 435, 927. doi:10.1051/0004-6361:20041817
- Evans, D. W., Riello, M., De Angeli, F., et al. 2018, *A&A*, 616, A4. doi:10.1051/0004-6361/201832756
- Gaia Collaboration, Brown, A. G. A., Vallenari, A., et al. 2018, *A&A*, 616, A1. doi:10.1051/0004-6361/201833051
- Gaia Collaboration, Babusiaux, C., van Leeuwen, F., et al. 2018, *A&A*, 616, A10. doi:10.1051/0004-6361/201832843
- Gao, X. 2020, *ApJ*, 894, 48. doi:10.3847/1538-4357/ab8560
- Gran, F., Minniti, D., Saito, R. K., et al. 2016, *A&A*, 591, A145. doi:10.1051/0004-6361/201527511
- Jacobson, H. R., Pilachowski, C. A., & Friel, E. D. 2011, *AJ*, 142, 59. doi:10.1088/0004-6256/142/2/59
- Jeffery, C. S. & Saio, H. 2016, *MNRAS*, 458, 1352. doi:10.1093/mnras/stw388
- Jayasinghe, T., Kochanek, C. S., Stanek, K. Z., et al. 2018, *MNRAS*, 477, 3145. doi:10.1093/mnras/sty838
- Johnson, H. L. & Morgan, W. W. 1953, *ApJ*, 117, 313. doi:10.1086/145697
- Joshi, Y. C., John, A. A., Maurya, J., et al. 2020, *MNRAS*, 499, 618. doi:10.1093/mnras/staa2881
- Kaluzny, J. & Mazur, B. 1991, *AcA*, 41, 279
- Krone-Martins, A. & Moitinho, A. 2014, *A&A*, 561, A57. doi:10.1051/0004-6361/201321143
- Layden, A. C. 1998, *AJ*, 115, 193. doi:10.1086/300195
- Lenz, P. & Breger, M. 2005, *Communications in Asteroseismology*, 146, 53. doi:10.1553/cia146s53
- Li, C.-Y., Esamdin, A., Zhang, Y., et al. 2021, *Research in Astronomy and Astrophysics*, 21, 068. doi:10.1088/1674-4527/21/3/068
- Lindgren, L., Hernández, J., Bombrun, A., et al. 2018, *A&A*, 616, A2. doi:10.1051/0004-6361/201832727
- Liu, L. & Pang, X. 2019, *ApJS*, 245, 32. doi:10.3847/1538-4365/ab530a

- Luo, A.-L., Zhao, Y.-H., Zhao, G., et al. 2015, *Research in Astronomy and Astrophysics*, 15, 1095.
doi:10.1088/1674-4527/15/8/002
- Luo, X., Zheng, S., Huang, Y., et al. 2022, *Research in Astronomy and Astrophysics*, 22, 015003. doi:10.1088/1674-4527/ac321d
- Ma, S.-G., Esamdin, A., Ma, L., et al. 2018, *Ap&SS*, 363, 68.
doi:10.1007/s10509-018-3289-y
- Ofir, A., Alonso, R., Bonomo, A. S., et al. 2010, *MNRAS*, 404, L99. doi:10.1111/j.1745-3933.2010.00843.x
- Oliveira, A. F., Monteiro, H., Dias, W. S., et al. 2013, *A&A*, 557, A14. doi:10.1051/0004-6361/201321157
- Phelps, R. L. & Janes, K. A. 1994, *ApJS*, 90, 31.
doi:10.1086/191857
- Piskunov, A. E., Kharchenko, N. V., Röser, S., et al. 2006, *A&A*, 445, 545. doi:10.1051/0004-6361:20053764
- Sandquist, E. L., Serio, A. W., & Shetrone, M. 2011, *AJ*, 142, 194.
doi:10.1088/0004-6256/142/6/194
- Shan, Z., Yang, J., Sanjuán, M. A. F., et al. 2022, *European Physical Journal Plus*, 137, 50.
doi:10.1140/epjp/s13360-021-02279-x
- Song, F.-F., Esamdin, A., Ma, L., et al. 2016, *Research in Astronomy and Astrophysics*, 16, 154.
doi:10.1088/1674-4527/16/10/154
- Soubiran, C., Odenkirchen, M., & Le Campion, J.-F. 2000, *A&A*, 357, 484
- Tamuz, O., Mazeh, T., & Zucker, S. 2005, *MNRAS*, 356, 1466.
doi:10.1111/j.1365-2966.2004.08585.x
- Tarricq, Y., Soubiran, C., Casamiquela, L., et al. 2021, *arXiv:2111.05291*
- Tody, D. 1986, *Proc. SPIE*, 627, 733. doi:10.1117/12.968154
- Tody, D. 1993, *Astronomical Data Analysis Software and Systems II*, 52, 173
- Turner, D. G. 1976, *AJ*, 81, 97. doi:10.1086/111858
- Turner, D. G. 1979, *PASP*, 91, 642. doi:10.1086/130556
- Uytterhoeven, K., Moya, A., Grigahcène, A., et al. 2011, *A&A*, 534, A125. doi:10.1051/0004-6361/201117368
- VanderPlas, J. T. & Ivezić, Ž. 2015, *ApJ*, 812, 18.
doi:10.1088/0004-637X/812/1/18
- Zhao, G., Zhao, Y.-H., Chu, Y.-Q., et al. 2012, *Research in Astronomy and Astrophysics*, 12, 723.
doi:10.1088/1674-4527/12/7/002